Title	Low-frequency optical phonon modes and carrier mobility in the halide perovskite CH3NH3PbBr3 using terahertz time-domain spectroscopy
Author(s)	Zhao, Daming; Skelton, Jonathan M.; Hu, Hongwei; La-o-vorakiat, Chan; Zhu, Jian-Xin; Marcus, Rudolph A.; Michel-Beyerle, Maria-Elisabeth; Lam, Yeng Ming; Walsh, Aron; Chia, Elbert E. M.
Citation	Zhao, D., Skelton, J. M., Hu, H., La-o-vorakiat, C., Zhu, J. -X., Marcus, R. A., et al. (2017). Low-frequency optical phonon modes and carrier mobility in the halide perovskite CH3NH3PbBr3 using terahertz time-domain spectroscopy. Applied Physics Letters, 111(20), 201903-.
Date	2017
URL	http://hdl.handle.net/10220/44183
Rights	

Low-frequency optical phonon modes and carrier mobility in the halide perovskite $CH_3NH_3PbBr_3$ using terahertz time-domain spectroscopy

Daming Zhao,[1] Jonathan M. Skelton,[2] Hongwei Hu,[3] Chan La-o-vorakiat,[4,5] Jian-Xin Zhu,[6,7] Rudolph A. Marcus,[1,8] Maria-Elisabeth Michel-Beyerle,[1] Yeng Ming Lam,[3] Aron Walsh,[2,9,10,a)] and Elbert E. M. Chia[1,b)]

[1]*Division of Physics and Applied Physics, School of Physical and Mathematical Sciences, Nanyang Technological University, Singapore 637371, Singapore*
[2]*Department of Chemistry, University of Bath, Claverton Down, Bath BA2 7AY, United Kingdom*
[3]*School of Materials Science and Engineering, Nanyang Technological University, Singapore 639798, Singapore*
[4]*Nanoscience and Nanotechnology Graduate Program, King Mongkut's University of Technology Thonburi, Bangkok 10140, Thailand*
[5]*Theoretical and Computational Science Center (TaCS), Faculty of Science, King Mongkut's University of Technology Thonburi, Bangkok 10140, Thailand*
[6]*Theoretical Division, Los Alamos National Laboratory, Los Alamos, New Mexico 87545, USA*
[7]*Center for Integrated Nanotechnologies, Los Alamos National Laboratories, Los Alamos, New Mexico 87545, USA*
[8]*Noyes Laboratory, California Institute of Technology, Pasadena, California 91125, USA*
[9]*Department of Materials, Imperial College London, Exhibition Road, London SW7 2AZ, United Kingdom*
[10]*Global E^3 Institute and Department of Materials Science and Engineering, Yonsei University, Seoul 03722, South Korea*

(Received 29 June 2017; accepted 2 November 2017; published online 16 November 2017)

As a light absorber in photovoltaic applications, hybrid organic-inorganic halide perovskites should have long and balanced diffusion lengths for both the separated electrons and holes before recombination, which necessitates high carrier mobility. In polar semiconductors, the room-temperature carrier mobility is often limited by the scattering between carriers and the lowest-frequency optical phonon modes. Using terahertz time-domain spectroscopy, we examine the temperature evolution of these phonon modes in $CH_3NH_3PbBr_3$ and obtained high carrier mobility values using Feynman's polaron theory. This method allows us to estimate the upper limit of carrier mobilities without the need to create photogenerated free carriers, and can be applied to other heteropolar semiconductor systems with large polarons. *Published by AIP Publishing.*
https://doi.org/10.1063/1.4993524

The lead halide perovskite family, $CH_3NH_3PbI_3$ ($MAPbI_3$), $MAPbBr_3$ and relatives, have attracted much interest as candidates for photo-absorbers in next-generation photovoltaic devices.[1–3] The highest power conversion efficiency of laboratory-scale devices has reached 22.1%,[4] as a result of broadband absorption in the solar spectrum, long-range balanced electron and hole diffusion lengths, and high carrier mobility.[5–7]

The $MAPbX_3$ (X = I, Br) compounds consist of two sub-lattices comprising an inorganic PbX_3 octahedral framework and MA^+ organic cations. First-principles calculations show that, in contrast to all-inorganic perovskites, hybrid organic–inorganic perovskites possess several unique properties, *viz.*, that the interband transition near the band edge is dominated by the electronic states of the inorganic framework, while symmetry breaking associated with the organic cation produces disorder in the material.[8–10]

Hybrid perovskites have been characterized by various experimental techniques including optical spectroscopy,[6,11,12] X-ray diffraction,[13] and neutron scattering.[14] Many optical techniques, such as photoluminescence (PL) spectroscopy and transient-absorption spectroscopy, study processes such as carrier recombination, carrier relaxation, and electron-phonon coupling indirectly, based on interband transitions on electron-volt energy scales. In contrast, as a direct way to elucidate the evolution of free carriers, recent terahertz (THz) spectroscopic studies illustrate that both free carriers and phonon modes coexist in the THz frequency range.[15,16] It is therefore important to study the lowest-lying phonon modes and their evolution with temperature, in order to characterise the transport and recombination processes in these materials.

In $MAPbX_3$, the orthorhombic-to-tetragonal phase transition is accompanied by the order-disorder behavior of the MA^+ cation orientation.[10,17] The THz response of $MAPbI_3$ has been studied both theoretically and experimentally,[16–18] whereas the bromide analogue $MAPbBr_3$ has received relatively less attention. The latter has been widely employed in mixed-cation and mixed-halide perovskites,[19] to improve the stability of all-perovskite tandem cells.

As a hybrid organic–inorganic crystal, the disorder of the organic MA^+ cation plays a key role in the phase transitions. The orientation of the C–N axis is fixed in the orthorhombic phase, while the dipole has various possible orientations in the tetragonal and cubic phases. Thus, the transition from orthorhombic to tetragonal is not only related to the change in the crystal structure and unit-cell volume but is also linked to the order-disorder transition. The structural phase transitions in single-crystal $MAPbBr_3$ are reported to take place at[10]

a)Electronic mail: a.walsh@imperial.ac.uk
b)Electronic mail: elbertchia@ntu.edu.sg

$$\text{ortho} \xrightleftharpoons{148.8\text{K}} \text{tetraII} \xrightleftharpoons{150.0\text{K}} \text{tetraI} \xrightleftharpoons{236.3\text{K}} \text{cubic}$$

In this paper, we study the temperature evolution of the phonon modes in $MAPbBr_3$ thin films from 20 to 300 K in the region of 0.3–2.8 THz. We observe that two peaks in the tetragonal and cubic phases split into three peaks in the orthorhombic phase, with the additional mode at 1.8 THz gradually appearing near the phase-transition temperature. Comparing our results with first-principles density-functional theory (DFT) calculations, we attribute the phonon-mode splitting to the orthorhombic-to-tetragonal phase transition.

The perovskite precursor solution was prepared by dissolving MABr and $PbBr_2$ in a stoichiometric ratio in dimethylformamide/dimethyl sulfoxide (4:1 v/v, 1 M) at 80 °C. The precursor solution was spin-coated onto a *z*-cut quartz substrate ($10 \times 10 \times 1$ mm) at 1000 rpm for 10 s and 4000 rpm for 30 s, with 250 μL of chlorobenzene being dripped onto the sample surface after 15 s during the second stage of the spin coating. Subsequently, the perovskite layer was annealed at 80 °C for 5 min and 100 °C for 10 min. The thickness of the polycrystalline $MAPbBr_3$ film was (932 ± 11) nm. The sample was kept under nitrogen before being mounted onto our THz-TDS system under vacuum (10^{-7} mbar), which was maintained throughout the measurements to minimize exposure of the sample to air.

Our THz spectrometer setup and data analysis method have been reported elsewhere.[16] The THz conductivity $\tilde{\sigma}(\omega) = \sigma_1(\omega) + i\sigma_2(\omega)$ is obtained from the relation $\tilde{\sigma}(\omega) = i\omega\epsilon_0[1 - \tilde{n}(\omega)^2]$, where $\tilde{n}(\omega) = n(\omega) + i\kappa(\omega) = \sqrt{\tilde{\epsilon}(\omega)}$ is extracted from the transmission function

$$\tilde{T}(\omega) = \frac{2\tilde{n}(\tilde{n}_{sub} + 1)\exp[i\omega d(\tilde{n} - 1)/c]\exp[-i\omega\Delta L(\tilde{n}_{sub} - 1)/c]}{(1 + \tilde{n})(\tilde{n} + \tilde{n}_{sub}) + (\tilde{n} - 1)(\tilde{n}_{sub} - \tilde{n})\exp[2i\omega d\tilde{n}/c]}, \quad (1)$$

where $\tilde{n}_{sub}$ is the complex refractive index of the substrate, d the sample film thickness, ΔL the difference in thickness of the sample and reference substrates, and c the speed of light in vacuum. Extraction of the refractive index using Eq. (1) yields exact solutions without resorting to the thin-film approximation.[20] As dipole oscillators, phonon modes show Lorentzian behavior, producing an absorption peak in the real part of the optical conductivity $\sigma_1(\omega)$, and rising up across zero in the imaginary part $\sigma_2(\omega)$ at the resonant frequency (Fig. 1). At 300 K, two phonon modes are observed at 1.35 THz (mode 1) and 2.19 THz (mode 2). These frequencies agree well with recent theoretical calculations, based on which mode 1 can be attributed to distortions of the octahedra due to changes in the Br–Pb–Br bond angles, and mode 2 to changes in the Pb–Br bond lengths.[21] We note that the calculations indicate the presence of multiple modes coexisting around these central frequencies [Fig. 2(a)]; this may be due in part to the cation breaking the symmetry of the "frozen" structure, and thus splitting modes that would be degenerate in the time-averaged cubic structure.

Above 150 K, the spectra are well fit by two Lorentzian oscillators, which is near the reported single-crystal-to-single-crystal tetragonal-to-orthorhombic phase transition temperature. Below 150 K, a shoulder feature at 1.8 THz (mode 3) gradually becomes a dominant peak at the lowest temperatures, necessitating the addition of a third Lorentzian function. This feature clearly indicates that the structural phase transition induces a phonon-mode splitting. A similar shoulder also appears in the mid-infrared spectra in the orthorhombic phase and is attributed to the organic cations at ~28 THz.[10] Although weak, three more modes at 0.7, 1.0, and 2.6 THz can only be identified below 150 K.

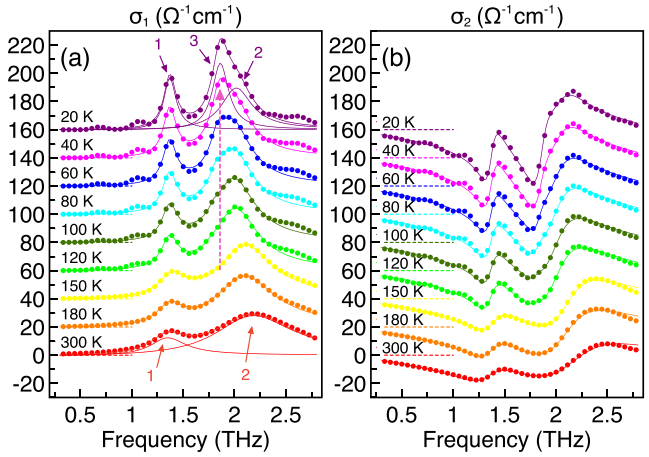

FIG. 1. Temperature-dependent THz conductivities of thin-film $MAPbBr_3$: (a) real part $\sigma_1(\omega)$ and (b) imaginary part $\sigma_2(\omega)$. Contributions from individual Lorentzian oscillators (solid lines) are plotted for $\sigma_1(\omega)$ at 20 K and 300 K. Two phonon modes (modes 1 and 2) are observed above 150 K, while one additional mode (mode 3) appears below 150 K due to the tetragonal–orthorhombic phase transition. The dashed arrow points to the appearance of the additional phonon mode 3. The data are offset vertically by horizontal dashed lines.

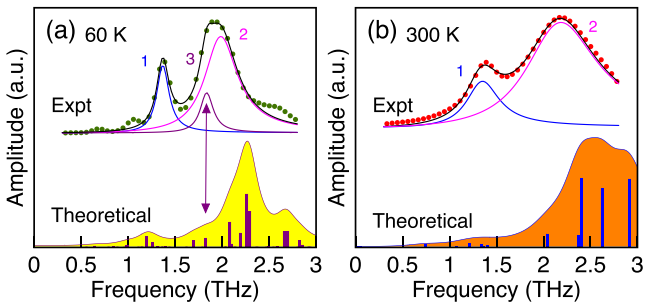

FIG. 2. Simulated THz spectra of $MAPbBr_3$ in the (a) orthorhombic and (b) cubic phases. The vertical sticks show the position and relative IR intensities of the phonon modes obtained from DFT calculations. By assuming a nominal 0.25 THz (orthorhombic phase) and 0.45 THz (cubic phase) linewidth for all the modes, simulated THz absorption spectra can be obtained (filled curves). In the orthorhombic phase, new phonon peaks appear between 1.5 and 2 THz, marked by an arrow in (a), in agreement with the experimental data (vertically shifted solid lines).

Although room-temperature THz data on $MAPbBr_3$ have been reported earlier,[22] we show here temperature-dependent THz measurements, which can show the fingerprints of structural phase transitions. To explore the possibility that the appearance of the shoulder/peak feature below 150 K is due to the tetragonal-to-orthorhombic phase transition, we performed DFT-based lattice-dynamics simulations of the THz spectra following a similar procedure to that in our previous work.[21,23] Data for cubic $MAPbBr_3$ was taken from our previous study.[21] An initial model of the orthorhombic phase was built from the optimized structure of the iodide analogue,[17,21,23] which was then fully optimized using the VASP code[24] with care taken to converge the electronic wavefunctions and forces (10^{-8} eV and 10^{-2} eVÅ^{-1}, respectively). We used the PBEsol exchange-correlation functional[25] with projector augmented-wave (PAW) pseudopotentials[26,27] with the outermost *s*, *p*, and Pb *d* electrons in the valence shell. A plane-wave cut-off of 800 eV was employed with a regular $3\times2\times3$ Γ-centered Monkhorst-Pack *k*-point mesh.[28] The precision of the charge-density grids was set automatically to avoid aliasing errors, and the PAW projection was performed in reciprocal space. The Γ-point phonon frequencies and eigenvectors and the atomic Born effective-charge tensors were then obtained using the density-functional perturbation theory, which were then combined to calculate the mode IR activities according to the method outlined in Skelton *et al.*[29]

From Fig. 2(a), we see that, in the orthorhombic phase, both the experimental and simulated spectra show two major peaks (labelled 1 and 2) and one shoulder (labelled 3). The shoulder results from the two weak IR-active phonon modes in the 1.5–2 THz range in the orthorhombic phase, which are absent in the cubic phase, in agreement with our measurements. The lattice dynamic calculations therefore support our observation that the shoulder feature is present only in the orthorhombic phase. We note that both sets of simulated spectra are blue-shifted to higher energies compared to the experimental measurements. Similar phenomena have been observed by Ahmed *et al.* in $MAPbI_3$.[31] More recently, high-quality Raman spectra, obtained from single-crystal $MAPbI_3$ and $MAPbBr_3$ samples,[11,21] also found that the calculated frequencies of the lowest-lying phonon modes were higher than those obtained from the measured Raman spectra.[21] This may be due in part to the fact that the spectra are simulated from the athermal 0 K structures—at finite temperature, thermal expansion of the lattice can result in a softening of the phonon frequencies and an increase in anharmonicity. It may also be partly due to the cation being frozen in one particular orientation in the model of the cubic phase, although this should not be an issue for the orthorhombic phase.

As noted earlier, we model the measured spectra, $\tilde{\sigma}(\omega)$, using a set of Lorentz oscillators, with two oscillators for spectra recorded above 150 K, and three for those taken below 150 K

$$\tilde{\sigma}(\omega) = -i\omega\epsilon_0(\epsilon_\infty - 1) + \sum_m \frac{\epsilon_0\omega_{p,m}^2\omega}{i(\omega_{TO,m}^2 - \omega^2) + \omega\gamma_m}, \quad (2)$$

where $\omega_{p,m}$, $\omega_{TO,m} = 2\pi f_m$ and γ_m are the oscillator strength, transverse optical (TO)-phonon frequency and linewidth of the *m*th oscillator, respectively. The high-frequency dielectric constant ϵ_∞ accounts for all dielectric contributions from beyond our experimental frequency window.

The temperatures of the tetraII-to-ortho (148.8 K) and tetraI-to-tetraII (154.0 K) transitions are very close to each other. The transition width can be as broad as ±20 K in thin-film samples,[32] and it is therefore most likely that all three phases—ortho, tetraI, and tetraII—coexist between 130 and 170 K. Note that we do not observe any significant signatures of structural phase transitions between the cubic, tetraI, and tetraII phases in the conductivity spectra.

The evolution of the fitted oscillator strengths of modes 2 and 3 with temperature is shown in Fig. 3(a). The combined oscillator strength of modes 2 and 3 [shown as a blue dashed line in Fig. 3(a)] is conserved below 140 K, suggesting that it is mode 2 in the tertaII phase that splits into modes 2 and 3 in the orthorhombic phase.

Note that peaks in $\sigma_1(\omega)$ gives the frequencies (ω_{TO}) and oscillator strengths of the TO phonon modes. Although distortions in the inorganic cages lead to local breaking of the space-group symmetry, which gives these TO phonon modes both TO and longitudinal optical (LO) character, we proceeded to plot the loss function $-\mathrm{Im}[1/\tilde{\epsilon}(\omega)]$ [which is the negative imaginary part of the complex response function $1/\tilde{\epsilon}(\omega)$], whose peaks more accurately determine the LO phonon mode frequency ω_{LO}.[33,34] Figure 3(b) shows the 300 K loss function data in red circles. Due to the frequency window of our setup, only one peak can be identified at 1.59 THz. However, since the fits to both the real and imaginary parts of $\tilde{\sigma}(\omega)$ have been obtained, we use the fitting parameters to compute the loss function up to 5 THz. The calculated loss function is shown as a black solid line in Fig. 3(b), showing two peaks at $\omega_{LO,1}/2\pi = 1.59$ THz and $\omega_{LO,2}/2\pi = 3.55$ THz. Note that the positions of these two peaks are consistent with the Cochran-Cowley relation[35]

$$\frac{\epsilon_{static}}{\epsilon_\infty} = \prod_{i=1}^{2}\frac{\omega_{LO,i}^2}{\omega_{TO,i}^2}, \quad (3)$$

where ϵ_{static} is the static dielectric constant, thus giving an independent confirmation of the accuracy of these two values (see the supplementary material for details). The second LO-phonon peak was observed at 5 THz by Sendner *et al.*,[22] which differs from our 3.55 THz value. In the supplementary material, the possible reasons for the discrepancy are described in detail, such as the uncertainty in the value of ΔL

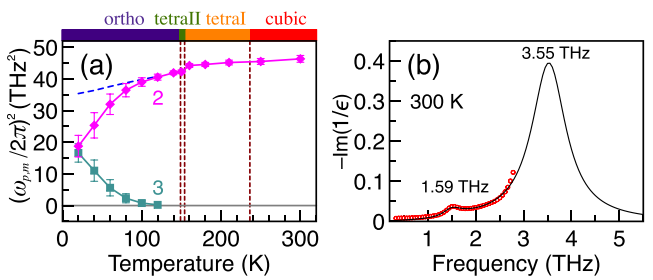

FIG. 3. (a) Evolution of oscillator strengths of mode 2 and 3 with temperature. Vertical dashed lines indicate the reported phase transition temperatures. The blue dashed line indicates the sum of oscillator strength of mode 2 and 3. (b) Measured (red circles) and extrapolated (black line) loss function $-\mathrm{Im}[1/\epsilon(\omega)]$ based on the fit of $\tilde{\sigma}(\omega)$ at 300 K.

TABLE I. Calculated 300 K carrier mobility based on carrier-LO phonon scattering in $MAPbBr_3$. The LO phonon mode frequencies are taken from the peaks in the loss function $-\mathrm{Im}[1/\tilde{\epsilon}(\omega)]$. The effective LO phonon mode frequency is obtained by the sum of weighted LO modes. Mobilities are calculated using the effective LO phonon mode.

Material	ϵ_∞	ϵ_{static}	$\omega_{LO,eff}/2\pi$	Carrier	m_b/m_0	α	w	v	μ ($\mathrm{cm^2\,V^{-1}\,s^{-1}}$)
$MAPbBr_3$	6.7	25	3.46 THz	e	0.25 (Ref. 30)	1.68	11.4	13.0	83
				h	0.12 (Ref. 30)	1.17	11.5	12.6	265

and the determination of LO phonon mode frequency outside the experimental frequency window.

In systems with multiple LO-phonon modes, Hellwarth *et al*. derived an *effective* LO mode frequency $\omega_{LO,eff}$ from the frequencies and weights of the individual modes. This value of $\omega_{LO,eff}$ is then used to calculate the carrier mobility according to Hellwarth's[36] and Feynman's[37] theories. In our case, we use two Lorentz oscillators to fit the complex response function to obtain the weight W_i^2 for each LO mode $\omega_{LO,i}$. We then obtain $\omega_{LO,eff}$ from[36]

$$\omega_{LO,eff}^2 = \sum_i W_{LO,i}^2 / \sum_i \left(\frac{W_{LO,i}^2}{\omega_{LO,i}^2}\right), \tag{4}$$

to finally obtain $\omega_{LO,eff} = 3.46$ THz in $MAPbBr_3$.

In photovoltaic applications, it is always desirable to have high photogenerated carrier mobility at room temperature. The reported values vary from 10 to 100 $\mathrm{cm^2\,V^{-1}\,s^{-1}}$, depending on the sample preparation method, measurement approaches, and corresponding assumptions.[38–40] One key question is that of whether there is an upper limit to the carrier mobility in hybrid perovskites.

In polar semiconductors, carrier mobility is limited by scattering with LO phonons. We estimate the upper limit of the carrier mobility using Feynman's polaron theory.[36,37] This theory has been applied to various semiconductor systems, such as halide perovskites,[16,41] InSb,[42] $Ca_{1-x}La_xMnO_3$,[43] TiO_2,[44] and $Bi_{12}SiO_{20}$.[45]

The carrier mobility, derived for large (Fröhlich) polarons, follows the expression[36,37]

$$\mu = \frac{w^3}{v^3}\frac{3e}{m_b}\frac{\sqrt{\pi}\sinh(\beta/2)}{\omega_{LO,eff}\alpha\beta^{5/2}}\frac{1}{K(a,b)}, \tag{5}$$

where e is the elementary charge, m_b the band effective mass of the electrons or holes, α the carrier-phonon coupling constant, and $\beta = \hbar\omega_{LO,eff}/k_BT$, with $\hbar$ the Planck constant, k_B the Boltzmann constant, and T the temperature. The factor $K(a, b)$ is a function of w and v: $K(a,b) \equiv \int_0^\infty du[u^2 + a^2 - b\cos(vu)]^{-3/2}\cos(u)$, where $a^2 = (\beta/2)^2 + R\beta\coth(\beta v/2)$, $b = R\beta\sinh(\beta v/2)$, and $R = (v^2 - w^2)/w^2v$.

The variational parameters w and v are obtained when the Osaka free energy achieves a minimum for a LO phonon at a particular temperature. We obtained the values of w and v for $\omega_{LO,eff}$, at 300 K.[36,37] The carrier-phonon coupling constants are calculated via $\alpha = \sqrt{m_b e^4/2\hbar^2\epsilon_*^2 E_{LO}}$, where $1/\epsilon_* = 1/\epsilon_\infty - 1/\epsilon_{static}$, $E_{LO} = \hbar\omega_{LO,eff}$,[46] and are listed in Table I. The electron-phonon coupling constant $\alpha_{e-ph} = 1.68$ agrees well with the value of 1.69 obtained from DFT calculations.[41] The small values of α (1–2) indicate that the system is in the large-polaron regime ($\alpha < 6$), and so justifies the use of Eq. (5) in our calculation of carrier mobility.

We summarize the parameters and calculated mobilities for electrons and holes in Table I. Mobilities of 10–100 $\mathrm{cm^2\,V^{-1}\,s^{-1}}$ obtained from measurements on single-crystals,[38,39] especially the high hole-mobility[40] (~210 $\mathrm{cm^2\,V^{-1}\,s^{-1}}$), agree well with our values. Note that Sendner *et al*.[22] performed the same analysis on $MAPbBr_3$ to obtain $\alpha = 1.69$. Also they used the reduced exciton mass in the mobility calculation to obtain $\mu = 158\,\mathrm{cm^2\,V^{-1}\,s^{-1}}$, whose value lies between our values of electron and hole mobilities.

From Eqs. (4) and (5), we see that the low-frequency THz modes make the largest contribution to the loss function, and therefore determine the effective frequency and, hence, upper limit to the carrier mobility. In real materials, carriers are also scattered by grain boundaries, defects, disorder,[15] and ion impurities,[47] and so the observed mobility will likely be smaller than our calculated upper limit. Note that our previous work on $MAPbI_3$ used the low-temperature expression from Feynman's theory, which calculated the low-temperature mobility, and therefore obtained values larger than those in this work.[16]

In conclusion, we have studied the THz phonon modes in the hybrid halide perovskite $MAPbBr_3$. Phonon mode splitting is observed at 150 K, which we attribute to the tetragonal–orthorhombic phase transition. We use Feynman's polaron theory to estimate the upper limit of the carrier mobility based on scattering with LO phonons, and obtain values that agree well with other measurements. Our method gives an upper limit to the carrier mobility from the knowledge of the low-frequency phonon modes, without the need to generate carriers via photoexcitation. This method can be applied to other polar semiconductors where LO phonon frequencies, carrier-phonon coupling constant, and band-effective mass are known.

See supplementary material for the discussions on the uncertainty in the calculated loss function, consistency with the Cochran-Cowley relation, why the lowest phonon modes dominate the carrier mobility, and the real part of the dielectric function at 300 K.

D.M.Z. acknowledges support from TUM-CREATE. E.E.M.C. acknowledges support from the Singapore Ministry of Education AcRF Tier 1 (RG123/14) and Tier 2 (MOE2015-T2-2-065 and MOE2016-T2-1-054). C.L. acknowledges support from the Theoretical and Computational Science (TaCS) Center and Thailand Research Fund (MRG6080264). R.A.M. thanks the ONR and ARO for their support. M.-E.M.-B. is grateful to the Nanyang Technological University for supporting the

Biophysics Center. The work was supported in part by the Center for Integrated Nanotechnologies, a U.S. DOE BES user facility. J.M.S. is grateful for support from the UK Engineering and Physical Sciences Research Council (EPSRC; Grant No. EP/P007821/1). Calculations were performed on the SiSu supercomputer at the IT Center for Science (CSC), Finland, via the Partnership for Advanced Computing in Europe (PRACE) Project No. 13DECI0317/IsoSwitch.

[1]A. Kojima, K. Teshima, Y. Shirai, and T. Miyasaka, J. Am. Chem. Soc. **131**, 6050 (2009).
[2]H. J. Snaith, J. Phys. Chem. Lett. **4**, 3623 (2013).
[3]H.-S. Kim, S. H. Im, and N.-G. Park, J. Phys. Chem. C **118**, 5615 (2014).
[4]See www.nrel.gov/ncpv/images/efficiency_chart.jpg for National Renewable Energy Laboratory. Research Cell Record Efficiency Chart.
[5]T. C. Sum and N. Mathews, Energy Environ. Sci. **7**, 2518 (2014).
[6]G. Xing, N. Mathews, S. Sun, S. S. Lim, Y. M. Lam, M. Grätzel, S. Mhaisalkar, and T. C. Sum, Science **342**, 344 (2013).
[7]S. D. Stranks, G. E. Eperon, G. Grancini, C. Menelaou, M. J. Alcocer, T. Leijtens, L. M. Herz, A. Petrozza, and H. J. Snaith, Science **342**, 341 (2013).
[8]F. Brivio, A. B. Walker, and A. Walsh, APL Mater. **1**, 042111 (2013).
[9]J. Ma and L.-W. Wang, Nano Lett. **15**, 248 (2015).
[10]N. Onoda-Yamamuro, T. Matsuo, and H. Suga, J. Phys. Chem. Solids **51**, 1383 (1990).
[11]O. Yaffe, Y. Guo, L. Z. Tan, D. A. Egger, T. Hull, C. C. Stoumpos, F. Zheng, T. F. Heinz, L. Kronik, M. G. Kanatzidis, J. S. Owen, A. M. Rappe, M. A. Pimenta, and L. E. Brus, Phys. Rev. Lett. **118**, 136001 (2017).
[12]Y. Yang, D. P. Ostrowski, R. M. France, K. Zhu, J. Van De Lagemaat, J. M. Luther, and M. C. Beard, Nat. Photonics **10**, 53 (2016).
[13]C. C. Stoumpos, C. D. Malliakas, and M. G. Kanatzidis, Inorg. Chem. **52**, 9019 (2013).
[14]I. Swainson, C. Stock, S. Parker, L. Van Eijck, M. Russina, and J. Taylor, Phys. Rev. B **92**, 100303 (2015).
[15]C. La-o-vorakiat, T. Salim, J. Kadro, M.-T. Khuc, R. Haselsberger, L. Cheng, H. Xia, G. G. Gurzadyan, H. Su, Y. M. Lam, R. A. Marcus, M.-E. Michel-Beyerle, and E. E. M. Chia, Nat. Commun. **6**, 7903 (2015).
[16]C. La-o-vorakiat, H. Xia, J. Kadro, T. Salim, D. Zhao, T. Ahmed, Y. M. Lam, J.-X. Zhu, R. A. Marcus, M.-E. Michel-Beyerle, and E. E. M. Chia, J. Phys. Chem. Lett. **7**, 1 (2016).
[17]L. D. Whalley, J. M. Skelton, J. M. Frost, and A. Walsh, Phys. Rev. B **94**, 220301 (2016).
[18]M. A. Pérez-Osorio, R. L. Milot, M. R. Filip, J. B. Patel, L. M. Herz, M. B. Johnston, and F. Giustino, J. Phys. Chem. C **119**, 25703 (2015).
[19]N. J. Jeon, J. H. Noh, W. S. Yang, Y. C. Kim, S. Ryu, J. Seo, and S. I. Seok, Nature **517**, 476 (2015).
[20]C. La-o vorakiat, L. Cheng, T. Salim, R. A. Marcus, M.-E. Michel-Beyerle, Y. M. Lam, and E. E. M. Chia, Appl. Phys. Lett. **110**, 123901 (2017).
[21]A. M. Leguy, A. R. Goñi, J. M. Frost, J. Skelton, F. Brivio, X. Rodríguez-Martínez, O. J. Weber, A. Pallipurath, M. I. Alonso, and M. Campoy-Quiles, Phys. Chem. Chem. Phys. **18**, 27051 (2016).
[22]M. Sendner, P. K. Nayak, D. A. Egger, S. Beck, C. Müller, B. Epding, W. Kowalsky, L. Kronik, H. J. Snaith, and A. Pucci, Mater. Horiz. **3**, 613 (2016).
[23]F. Brivio, J. M. Frost, J. M. Skelton, A. J. Jackson, O. J. Weber, M. T. Weller, A. R. Goni, A. M. Leguy, P. R. Barnes, and A. Walsh, Phys. Rev. B **92**, 144308 (2015).
[24]G. Kresse and J. Hafner, Phys. Rev. B **47**, 558 (1993).
[25]J. P. Perdew, A. Ruzsinszky, G. I. Csonka, O. A. Vydrov, G. E. Scuseria, L. A. Constantin, X. Zhou, and K. Burke, Phys. Rev. Lett. **100**, 136406 (2008).
[26]P. E. Blöchl, Phys. Rev. B **50**, 17953 (1994).
[27]G. Kresse and D. Joubert, Phys. Rev. B **59**, 1758 (1999).
[28]H. J. Monkhorst and J. D. Pack, Phys. Rev. B **13**, 5188 (1976).
[29]J. Skelton, L. Burton, A. Jackson, F. Oba, S. Parker, and A. Walsh, Phys. Chem. Chem. Phys. **19**, 12452 (2017).
[30]Y. H. Chang, C. H. Park, and K. Matsuishi, J. Korean Phys. Soc. **44**, 889 (2004).
[31]T. Ahmed, C. La-o-vorakiat, T. Salim, Y. M. Lam, E. E. M. Chia, and J.-X. Zhu, Europhys. Lett. **108**, 67015 (2015).
[32]V. D'Innocenzo, G. Grancini, M. J. Alcocer, A. R. S. Kandada, S. D. Stranks, M. M. Lee, G. Lanzani, H. J. Snaith, and A. Petrozza, Nat. Commun. **5**, 3586 (2014).
[33]R. Lowndes, Phys. Rev. B **1**, 2754 (1970).
[34]R. Huber, C. Kübler, S. Tübel, A. Leitenstorfer, Q. Vu, H. Haug, F. Köhler, and M.-C. Amann, Phys. Rev. Lett. **94**, 027401 (2005).
[35]W. Cochran and R. Cowley, J. Phys. Chem. Solids **23**, 447 (1962).
[36]R. W. Hellwarth and I. Biaggio, Phys. Rev. B **60**, 299 (1999).
[37]R. Feynman, R. Hellwarth, C. Iddings, and P. Platzman, Phys. Rev. **127**, 1004 (1962).
[38]M. I. Saidaminov, A. L. Abdelhady, B. Murali, E. Alarousu, V. M. Burlakov, W. Peng, I. Dursun, L. Wang, Y. He, and G. Maculan, Nat. Commun. **6**, 7586 (2015).
[39]D. Shi, V. Adinolfi, R. Comin, M. Yuan, E. Alarousu, A. Buin, Y. Chen, S. Hoogland, A. Rothenberger, and K. Katsiev, Science **347**, 519 (2015).
[40]H. Wei, Y. Fang, P. Mulligan, W. Chuirazzi, H.-H. Fang, C. Wang, B. R. Ecker, Y. Gao, M. A. Loi, and L. Cao, Nat. Photonics **10**, 333 (2016).
[41]J. M. Frost, Phys. Rev. B **96**, 195202 (2017).
[42]R. Agrawal, S. Dubey, and S. Ghosh, J. Phys.: Conf. Ser. **365**, 012045 (2012).
[43]J. Cohn, C. Chiorescu, and J. Neumeier, Phys. Rev. B **72**, 024422 (2005).
[44]E. Hendry, F. Wang, J. Shan, T. F. Heinz, and M. Bonn, Phys. Rev. B **69**, 081101 (2004).
[45]M. Wintermantel and I. Biaggio, Phys. Rev. B **67**, 165108 (2003).
[46]E. Menéndez-Proupin, P. Palacios, P. Wahnón, and J. Conesa, Phys. Rev. B **90**, 045207 (2014).
[47]T. Zhao, W. Shi, J. Xi, D. Wang, and Z. Shuai, Sci. Rep. **6**, 19968 (2016).